Eurographics Workshop on Visual Computing for Biology and Medicine (2020)
B. Kozlíková, M. Krone, and N. N. Smit (Editors)

InShaDe: Invariant Shape Descriptors for visual analysis of histology 2D cellular and nuclear shapes

M. Agus[1], K. Al-Thelaya[1], C. Calì[2], M. M. Boido[2], Y. Yang[1], G. Pintore[3], E. Gobbetti[3], and J. Schneider[1]

[1] College of Science and Engineering, Hamad Bin Khalifa University, Qatar
[2] NICO, University of Turin, Italy
[3] Visual Computing, CRS4, Italy

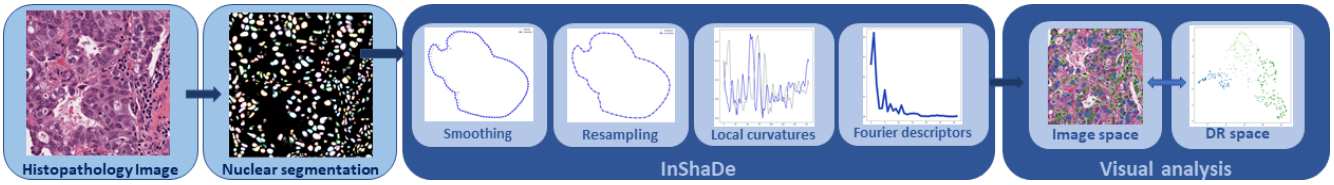

Figure 1: ***InShaDe:*** *from cell contours extracted from digital histology images, our pipeline computes invariant energy curvature-based Fourier descriptors. These synthetic descriptors can be used for visual analysis, proof-reading segmentation results, and domain-specific clustering according to specific taxonomies.*

Abstract

We present a shape processing framework for visual exploration of cellular nuclear envelopes extracted from histology images. The framework is based on a novel shape descriptor of closed contours relying on a geodesically uniform resampling of discrete curves to allow for discrete differential-geometry-based computation of unsigned curvature at vertices and edges. Our descriptor is, by design, invariant under translation, rotation and parameterization. Moreover, it additionally offers the option for uniform-scale-invariance. The optional scale-invariance is achieved by scaling features to z-scores, while invariance under parameterization shifts is achieved by using elliptic Fourier analysis (EFA) on the resulting curvature vectors. These invariant shape descriptors provide an embedding into a fixed-dimensional feature space that can be utilized for various applications: (i) as input features for deep and shallow learning techniques; (ii) as input for dimension reduction schemes for providing a visual reference for clustering collection of shapes. The capabilities of the proposed framework are demonstrated in the context of visual analysis and unsupervised classification of histology images.

CCS Concepts

• ***Applied computing*** → ***Imaging;*** • ***Computing methodologies*** → ***Shape representations;*** *Cluster analysis;*

1. Introduction

The last decades have witnessed the rapid improvement and proliferation of high-throughput digital acquisition technology capable to provide high-quality representations of real-world scenes and objects in many application domains. In particular, in biology and medicine the rise of whole-slide scanners and the digitization of traditional, confocal, and electron microscopy has led to the definition and application of wholly digital analysis methods and to the creation of large image databases [BAMC20]. While early uses of this technology in research and clinical practice were mostly for telepathology, second opinions, and education, in which the use of the digital data closely mimicked traditional processes, in recent years efforts have shifted towards exploiting the large amount of information embedded in the acquired images, and in image collections, to develop novel data-driven analysis and synthesis methods [ML16]. In this context, a wide array of basic tools are employed, ranging from the usage of handcrafted feature descriptors to fully data-driven approaches, to the mixing and matching of various approaches [KJ*18]. Especially in the context of digital pathology and biology, machine learning technologies, and in particular deep learning approaches, have achieved significant successes, demonstrating for instance their capability to provide automatic tools for segmentation and labelng thousands of cellular entities from single microscope images [CTT*19, GKB*19]. However, current purely data-driven frameworks suffer of a lack of tools for proofreading the segmented images, as well as for applying classification, filter-

DOI: 10.2312/vcbm.20201173

ing, computation, and visual exploration based on specific domain knowledge and taxonomies [TJL*20]. For this reasons, many applications require the use of descriptors that, by design, preserve some domain-specific characteristics. In this context, a key to better exploit the powerful capabilities of the novel learning frameworks is to not fully dismiss the designing of features, but to find ways to effectively integrate them with powerful descriptive models. In addition to expanding flexibility of usage, especially when human analysis is required, this approach could increase discrimination performance through incorporation of domain knowledge, and lighten the training efforts, in terms of data required and computational power.

Inspired by these considerations, we propose a novel visual analysis pipeline based on discrete differential geometry concepts, whose recent findings provide very powerful theoretical formulations for describing 2D and 3D shapes [BSSZ08, CW17]. The framework is based on a 2D curves and shape descriptor, which can be used in various application domains to complement or enhance generic based deep learning networks, such as U-Net [RFB15]. The descriptor, dubbed *InShaDe*, is based on the concept of discrete curvature of closed resampled contours, and it is determined by computing the approximating vertex osculating circles and edge osculating circles, and by intertwining the correspondent radii. In this way, we obtain a description of 2D curves that is naturally invariant with respect to rigid body transformations (translations and rotations). In order to apply the proposed geometry descriptor to cellular shapes extracted from histopathology images, we further process it in a way to ensure scaling invariance, through standard (z-)scores, as well as shift invariance, through Fourier analysis, by computing energy-based elliptic Fourier descriptors.

Hence, the main contributions of this work are the following:

- a robust geometry processing pipeline for computing 2D shape invariant descriptors exploiting shift-based interpolation and discrete differential geometry schemes;
- the visual mapping of 2D cellular contours to the shape descriptor embedding, based on modern dimensionality reduction schemes, like UMAP [MHM18].

We provide preliminary results to show how the proposed pipeline can be used in the context of proofreading and visual unsupervised classification of various histology images in different contexts, from medical diagnostics to neuroscience investigation.

2. Related Work

Our work deals with shape feature extraction from closed contours and with the analysis of histopathology images. These are very broad topics and a full coverage of the state-of-the-art is out of the scope of this paper. We refer the reader to various surveys and reviews on 2D shape analysis [MKJ08, KJ*18] and digital histopathology analysis [IVRR13, XY16, JR17] for having a comprehensive overview of the related fields. In the following, we discuss the methods that are most closely related to our approach.

Shape feature descriptors During last two decades, significant research efforts have been carried out in both the theoretical and the practical aspects of the shape-based image retrieval problem [KJ*18]. There are two main modeling approaches for representing shapes: region-based methods and boundary-based ones. Region-based techniques use moment descriptors to describe shapes, like geometrical moments [XL08], Zernike moments [KH90], Legendre moments [SLB*00], and Tchebichef moments [MOL01]. Although region-based approaches are global in nature and can be applied to generic shapes, boundary-based techniques appear to be more efficient for handling objects that can be described by their object contours. In this latter category a number of boundary-based techniques have been proposed in the literature, including Fourier descriptors [ZL03], Curvature Scale Space (CSS) [Mok95] , and wavelet descriptors [LTN06]. Our descriptor combines the features of curvature analysis together with Fourier analysis, similarly to what was proposed by El Ghazal et al. [EgBB08,EgBB12]. Differently from them, our method is based on recent findings in discrete differential geometry [Bob15], thus resulting in a more robust formulation with respect to the sampling strategy and to better classification results. On the orthogonal side, for the general classification problem, the exploitation of large amounts of data by machine learning strategies has led to significant advances [CFG*15, WSK*15]. Many current efforts attempt to work directly on raw data images [WLG*17, YSGG17], by designing deep neural networks in which the modeling is hidden in the network design and training strategy and the feature computation and filtering of information is automatically performed by the network. In parallel, in order to simplify classification and automatic shape generation, attempts to reduce the depth of networks by introducing meaningful parameterizations or embeddings of input shapes are gaining interest, since such parameterizations can simplify the automatic classification or shape generation (model-based or "shallow" learning) and reduce the number of training examples [SBR16]. Our work goes towards that direction, since we propose a simplified contour description that can be used either for supporting machine learning frameworks and for supervised visual analysis. In this work, we focus on the latter aspect.

Histology analysis Digital pathology and microscopy image analysis is widely used in the biomedical domain for comprehensive studies of cell morphology or tissue structure. In most cases, analysis is carried out through manual assessment, which is labor intensive and prone to inter-observer variations. Computer-aided systems have recently attracted a great deal of interest since they can dramatically reduce the manual efforts and increase reproducibility [XY16]. Among the various parts composing a computer-aided diagnosis system, nucleus or cell detection and segmentation play a key role to describe the molecular and morphological information underlying the investigated samples [XY16, RRDM08]. In the past few decades, many efforts have been devoted to automated nucleus/cell detection and segmentation, and an independent field named computational pathology (CPath) emerged simultaneously to the rapid proliferation of deep learning (DL) models for quantitative analysis of spatial patterns in digitized whole-slide images (WSIs) of cancerous tissue slides [GKG*20]. In this context, various medical studies have already demonstrated the potential of deep learning (DL) models in detecting neoplastic tissues and recognizing diagnostically relevant structures [NFL*19]. Very recently, particularly performing neural networks were proposed, like the U-Net architecture [RFB15], which operates on the entire im-

age and jointly infers the label at each pixel simultaneously, leading to more spatially coherent segmentation. U-Nets have been shown to achieve improved accuracy on several bioimage segmentation tasks, even when the data set is relatively small [RFB15]. The architecture has been improved in the context of nuclear segmentation on histopathology images [CTT*19], by enforcing equivariance to groups, specifically rotation and translation, similarly to group-equivariant CNNs (GCNNs) [CW16]. Moreover, in order to attract efforts to particular datasets or tasks in medical imaging, various challenge contests and public datasets have been published [KVA*19, GKG*20]. However, as now, segmentation and classification accuracy is still far from being accepted for clinical practice [SA20], and proofreading efforts from domain scientists are still required to double-check labeling consistency and segmentation accuracy [TJL*20]. Our pipeline goes towards that direction by providing a visual analysis framework that support digital pathologists to efficiently carry out investigations over labeling and segmentation quality. In this context, our proposed framework takes as input the automatic segmentation obtained from U-Net like networks [CTT*19], and it allows for visual analysis of the reduced parameter space obtained by performing dimension reduction over our Fourier-based contour shape descriptor.

3. Method

The input to our InShaDe pipeline are segmented nuclear envelopes of cells obtained by applying an U-Net [CTT*19] on microscopic histopathology images (see Figure 1). We then extract closed contours (3.1) from each segmentation mask and perform the following processing steps (see Figure 1 for a schematic representation):

(3.2) contour smoothing,
(3.3) geodesically uniform resampling,
(3.4) discrete curvature computation,
(3.5) feature scaling using standard (z-)scores (optional),
(3.6) embedding to constant dimensions,
(3.7) elliptic Fourier analysis (EFA).

Contour smoothing serves to reduce pixelation noise, whereas geodesically uniform resampling removes sampling biases and is a pre-requisite to computing discrete curvatures using discrete differential geometry formulations using osculating circles. Embedding the resulting descriptors in constant dimensions helps in removing noise and spurious frequencies during the EFA stage, but is also necessary to allow for easy comparison between shapes using, e.g., cosine or Euclidean metrics. The Fourier analysis is used to remove shift (i.e., choice of origin) from the parameterization of the closed curve. So far the resulting descriptor is invariant under translation and rotation (3.4) and invariant under parameterization shift (3.7). In addition, the optional feature scaling step (3.5) ensures invariance under uniform scaling. In our result section, we furthermore show how the final descriptor can be used in combination with dimensionality reduction schemes for visualizing clusters of nuclear shapes with similar geometric characteristics.

3.1. Contour Extraction & Chordal Parameterization

Given a segmentation mask, we extract a closed contour enveloping each nucleus using iso-contouring (specifically Marching Squares, which is a special case of Marching Cubes algorithm [LC87]). We reject open contours (i.e., the nucleus intersects the image boundary) and contours falling into the lowest 5% with respect to their number of samples. Let $\mathcal{C} := \{\mathbf{p}_i\}_1^N$, a closed curve with N vertices $\mathbf{p}_i$. We let $\Delta_i := \mathbf{p}_{i+1} - \mathbf{p}_i$, the i^{th} edge, consistent with Bobenko [Bob15], and abbreviate $l_i := \|\Delta_i\|_2$ (edge length). We then obtain an initial chordal parameterization $t(\mathcal{C})$ with $t_1 := t(\mathbf{p}_1) = 0$ and $t_{i+1} := t(\mathbf{p}_{i+1}) = \|\Delta_i\|_2 + t_i \; \forall \, i > 1$.

3.2. Contour Smoothing

The discrete nature of binary segmentation masks may lead to pixelation artifacts in the extracted contour. To prevent the resulting high spikes in curvature, we pre-smooth contours iteratively, using a superscript $\star^{(k)}$ to denote quantities at iteration k. The process is shown in Fig. 2. Specifically, we replace each vertex with a length-weighted average of the bisector of adjacent edges,

$$\mathbf{p}_i^{(k+1)} = \frac{l_i^{(k)} \left(\mathbf{p}_{i+1}^{(k)} + \mathbf{p}_i^{(k)}\right) + l_{i-1}^{(k)} \left(\mathbf{p}_i^{(k)} + \mathbf{p}_{i-1}^{(k)}\right)}{2\left(l_i^{(k)} + l_{i-1}^{(k)}\right)}. \tag{1}$$

As shown by Gottschalk [Got00], this sum of of length-weighted

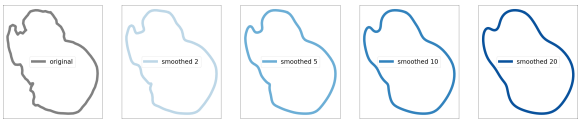

Figure 2: ***Contour smoothing:*** *we apply iterative contour smoothing to the closed contours (here, N=271) extracted from histology images. The higher the number of iteration steps, the smoother the contours: in the example, 2, 5,10, 20 steps respectively.*

edge bisectors computes the barycenter of the points on the piecewise linear curve segment $\mathbf{p}_{i-1}, \mathbf{p}_i, \mathbf{p}_{i+1}$. Since it is a 2-stage convex combination of $\mathbf{p}_{i-1}, \mathbf{p}_i, \mathbf{p}_{i+1}$, it is numerically stable and robust. Similar to virtually all smoothing operators, this does not yet preserve area. We therefore compute the area $a^{(0)}$ enclosed by the curve prior to smoothing and the area $a^{(k)}$ after each iteration. We then scale the curve by

$$\mathbf{p}_i^{(k)} \leftarrow \mathbf{p}_i^{(k)} \sqrt{\frac{a^{(0)}}{a^{(k)}}}. \tag{2}$$

3.3. Geodesically Uniform Resampling

In order to remove sampling bias and to employ discrete differential geometry formulations for vertex and edge curvature, we perform geodesically uniform resampling. We do so by placing equidistant samples $\widetilde{\mathbf{p}}$ on the piece-wise linear curve $\mathcal{C}$, thereby yielding a new piece-wise linear curve $\widetilde{\mathcal{C}}$ that is arc-length parameterized with respect to a unit scale u. Starting at a point $\mathbf{p}_1 = \widetilde{\mathbf{p}}_1$ and $u = 1$, we intersect the edges of $\widetilde{\mathcal{C}}$ with a unit circle around $\mathbf{p}_1$. This yields between zero and two intersection. If we find two intersections, we select one intersection as $\widetilde{\mathbf{p}}_2$ and keep track of the last edge, $\widetilde{\Delta}_1 = \widetilde{\mathbf{p}}_2 - \widetilde{\mathbf{p}}_1$. We then continue intersecting linear segments with unit spheres, but when deciding on $\widetilde{\mathbf{p}}_i$, we chose the intersection that maximizes $\left\langle \widetilde{\Delta}_i \, , \, \widetilde{\Delta}_{i-1} \right\rangle$, with $\widetilde{\Delta}_i$ defined analogously to $\widetilde{\Delta}_1$.

This enforces progress along the curve and prevents jumping back and forth on the curve. For our data, we did not encounter the case of finding less than two circle-curve intersections. Zero crossings would correspond to extremely small contours that cover less than a few pixels after processing; and we remove the bottom 5% shortest curves. One crossing would arise if part of the contour degenerates into a double line segment; Marching Squares does not extract such pathological curves.

Once the best intersection $\widetilde{\mathbf{p}}_{\widetilde{N}}$ "laps" past $\widetilde{\mathbf{p}}_1$, we use $\widetilde{\mathbf{p}}_{\widetilde{N}} = \widetilde{\mathbf{p}}_1$ instead to close the loop. This means that the last edge $\widetilde{\Delta}_{\widetilde{N}-1}$ may be shorter than unit length. In order to resolve this issue, we now calculate the length L of the curve. Knowing that $\|\widetilde{\Delta}_i\|_2 = u$ for all but the last edge, we have $L = \left(\widetilde{N}-2\right)u + \|\widetilde{\Delta}_{\widetilde{N}}\|_2$. To obtain an u for which $u^{-1}L$ is approximately integral, we round $u^{-1}L$ to the nearest integer L' and update $u \leftarrow L'^{-1}L$.

We then revert to placing samples along the original curve $\mathcal{C}$ with the updated spacing u. We repeat this process until the rounding error $\rho = |u^{-1}L - L'|$ (using the old u and the updated L') becomes negligibly small. In all of our experiments, three to five iterations reduced ρ to less than 10^{-4}. Given any number $x \in \mathbb{R}^0$, rounding to the nearest integer changes x by 0.25 on average. We therefore expect that $|1-u| \approx 0.25L^{-1}$, which we see confirmed in our experiments with typical contour lengths of more than 100 pixel widths (for reference, $L = 100 \rightarrow |1-u| \approx 2.5 \times 10^{-3}$). The result of this step is a new piece-wise linear curve $\widetilde{\mathcal{C}}$ that is arc-length parameterized with respect to a close-to-unit scale u.

3.4. Discrete Curvatures

For a discrete arc-length parameterized curve, there are two definitions of discrete curvature based on osculating circles [Bob15] (Section 2.3 therein). By defining the turning angle at vertex $\mathbf{p}_i$ as

$$\phi_i \equiv \arccos\langle \Delta_i, \Delta_{i-1} \rangle, \tag{3}$$

and by embedding the planar curve in the $z = 0$ plane (see also Fig. 3), we obtain for the (unsigned) **vertex curvature**:

$$\kappa_v = 2\frac{|\sin\varphi_i|}{\|\mathbf{p}_{i+1} - \mathbf{p}_{i-1}\|_2} = 2\frac{\|\Delta_i \times \Delta_{i-1}\|_2}{\|\Delta_i + \Delta_{i-1}\|_2}. \tag{4}$$

For the **edge curvature** we use the standard equation in [Bob15]:

$$\kappa_e = \frac{1}{\|\Delta_i\|_2}\left(\tan\frac{\phi_i}{2} + \tan\frac{\phi_{i+1}}{2}\right). \tag{5}$$

The choice to use unsigned vertex curvature was made to be consistent with the unsigned edge curvature. Using such a discrete differential geometry approach results in much more robust and stable curvature estimates than by using an intermediate interpolating spline. A reason may be that splines tend to over- and undershoot near vertices, and are thus not representative of the curvature in these points. Since one of our goals for the final shape descriptor is *optional* scale-invariance, we still have to scale curvatures back from our arbitrary unit length u to $u = 1$. This is achieved by dividing each κ_v and κ_e by u. Finally, we interleave vertex and edge curvatures to obtain a high-resolution, coherent descriptor. After this step, we also abandon the notion of curvature "living" on vertices and edges and transition to the notion that the shape descriptor

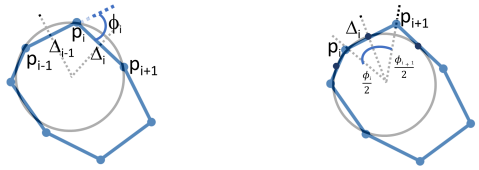

Figure 3: ***Discrete curvatures:*** *following discrete differential geometry [Bob15] we compute discrete curvatures by considering vertex osculating circles (left), and edge osculating circles (right).*

computed so far is a vector in a high-dimensional vector space. We also adopt the notion that this vector represents a 1D periodic signal on a uniform grid on the 2D circle. This interpretation is crucially supported by the fact that all edges have the same length prior to computing curvature. The descriptor computed so far is invariant under translation and rotation, but neither paramtric shift nor scale. We now establish the optional scale-invariance followed by shift-invariance.

3.5. Feature Scaling

Given a sequence of curvatures, $\{\kappa_i\}_{i=1}^{2\widetilde{N}}$, we compute standard scores (also called z-scores) by mapping

$$\kappa_i \leftarrow \frac{\kappa_i - \mu_\kappa}{\sigma_\kappa}, \tag{6}$$

where

$$\mu_\kappa = \frac{1}{2\widetilde{N}}\sum_{i=1}^{2\widetilde{N}}\kappa_i \quad \text{and} \quad \sigma_\kappa = \frac{1}{2\widetilde{N}-1}\sum_{i=1}^{2\widetilde{N}}(\kappa_i - \mu_\kappa)^2 \tag{7}$$

are the empiric mean and variance, respectively. Such a scaling is commonly employed in statistics as well as in training convolutional neural networks. However, normally standard scores are computed using global moments derived from the entire data set. This, in turn, does not provide full scale-invariance, since vectors with pre-dominantly small components will stay small. In contrast, by computing individual standard scores we enforce the optional scale-invariance of our descriptor as the bulk of the resulting coefficients are expected to be in the range $[-3,3]$ (normal distribution assumption).

3.6. Constant Dimensionality

Resampling the contour to a constant dimensionality as depicted in Fig. 4 allows us to control the number of elliptic harmonics in our Elliptic Fourier Analysis in a way to agree with the Nyquist sampling constraint. It is also a pre-requisite for easy comparison of shape descriptors using, e.g., cosine and Euclidean metrics. As an added side-benefit, it also allows us to eliminate remaining traces of noise on the curve. In this paper, we perform this resampling step based on shifted-linear interpolation [BTU04] for the following reasons: (i) shifted linear interpolation achieves performances that compare favourable to cubic interpolation at a much lower computational cost, (ii) shifted-linear interpolation is still convex, albeit with respect to shifted samples. It is thus free of oscillations

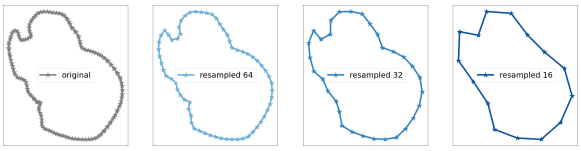

Figure 4: ***Resampling to constant dimension:*** *to reduce noise and spurious frequencies during the Fourier analysis and to enforce constant dimensionality of our descriptor, we apply uniform resampling through shifted linear interpolation [BTU04]. In this example, we show resampling with 64, 32 and 16 points respectively.*

and the amount of foreign frequencies introduced by resampling can be computed easily.

The basic idea of shifted-linear interpolation is to sample the original signal at positions other than the original underlying sampling grid, followed by standard linear interpolation. Blu et al. prove, somewhat surprisingly, that there is a data-independent and thus constant shift $\tau \approx 0.21$ that results in L^2-optimal reconstruction of the unknown original signal given only the known samples [BTU04]. Samples κ'_i at shifted positions t'_i are obtained using the infinite impulse response scheme described by Blu et al.,

$$\kappa'_i = -\frac{\tau}{1-\tau}\kappa'_{i-1} + \frac{1}{1-\tau}\kappa_i. \tag{8}$$

It should be noted, however, that linear interpolation on κ' is literally shifted "to the right" by τ, meaning that a sample $\kappa'(t)$ corresponds to $\kappa(t-\tau)$. The resulting interpolation thus becomes a shifted discrete convolution of the hat kernel

$$H(t) := \begin{cases} 1-|t| & \text{if } |t|<1 \\ 0 & \text{otherwise,} \end{cases} \tag{9}$$

with the shifted discrete signal κ':

$$\kappa(t) = \sum_i \kappa'_i H(t - t_i - \tau). \tag{10}$$

3.7. Elliptic Fourier Analysis (EFA)

To achieve shift-invariance (i.e., invariance under choice of parametric origin), we consider the Fourier spectrum of each given curve. In particular, we compute elliptic Fourier descriptors [SM06], similarly to what was proposed by Khazhdan et al. [KFR03] and successfully applied in various applications [AVG*19, AGP*20, DZPG89].

For a piecewise linear, periodic function $\kappa(t)\, t \in [0, 2\pi]$ representing the curvature of a contour, its Fourier elliptic expansion is obtained through linear combination of elliptic harmonics functions which provide a complete orthonormal basis for the decomposition

$$\kappa(t) = a_0 + \sum_{n=1}^{\infty}\left(a_n \cos\left(\frac{2\pi n t}{T}\right) + b_n \sin\left(\frac{2\pi n t}{T}\right)\right). \tag{11}$$

In order to compute the coefficients for the curvature function $\kappa(t)$ representing closed contours, we normalize the parameterization t to the interval $[0, 2\pi]$. As we are concerned with closed contours, the assumption of periodicity, $t = 0 \equiv 2\pi$ is naturally supported. We then consider the classic method proposed by Kuhl and Giardina [KG82]. This method essentially equates the discrete time derivative of Eqn. (11), at locations $\mathbf{p}_i$,

$$\dot{\kappa}_i := \left.\frac{\partial \kappa}{\partial t}\right|_{t_i} :$$
$$\dot{\kappa}_i = \frac{2\pi n}{T}\sum_{n=1}^{\infty}\left(-a_n \sin\left(\frac{2\pi n t_i}{T}\right) + b_n \cos\left(\frac{2\pi n t_i}{T}\right)\right), \tag{12}$$

with a Fourier expansion of the time derivative of the curvature,

$$\dot{\kappa}_i = \sum_{n=1}^{\infty}\left(a_n \cos\left(\frac{2\pi n t_i}{T}\right) + b_n \sin\left(\frac{2\pi n t_i}{T}\right)\right). \tag{13}$$

Noting that in Eqn. (13)

$$a_n = \frac{2}{T}\sum_{i=1}^{N}\dot{\kappa}_i\left(\sin\left(\frac{2\pi n t_i}{T}\right) - \sin\left(\frac{2\pi n t_{i-1}}{T}\right)\right) \text{ and}$$
$$b_n = \frac{2}{T}\sum_{i=1}^{N}\dot{\kappa}_i\left(\cos\left(\frac{2\pi n t_i}{T}\right) - \cos\left(\frac{2\pi n t_{i-1}}{T}\right)\right), \tag{14}$$

Kuhl and Giardina derive the following for the n^{th} harmonic.

$$a_n = \frac{T}{2\pi^2 n^2}\sum_{i=1}^{N}\dot{\kappa}_i\left(\cos\left(\frac{2\pi n t_i}{T}\right) - \cos\left(\frac{2\pi n t_{i-1}}{T}\right)\right) \text{ and}$$
$$b_n = \frac{T}{2\pi^2 n^2}\sum_{i=1}^{N}\dot{\kappa}_i\left(\sin\left(\frac{2\pi n t_i}{T}\right) - \sin\left(\frac{2\pi n t_{i-1}}{T}\right)\right). \tag{15}$$

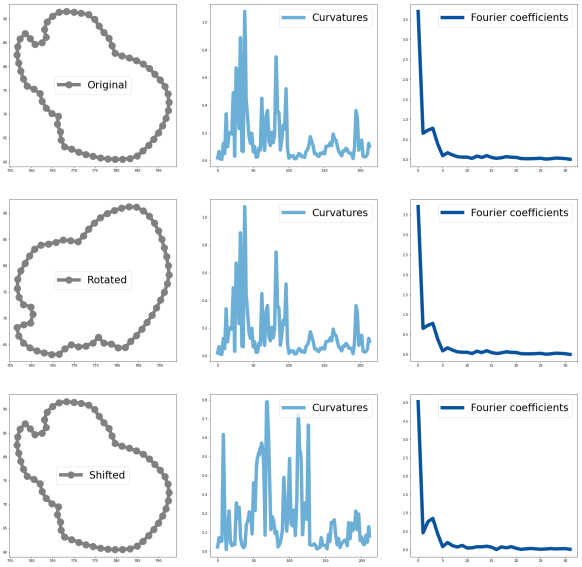

Figure 5: ***Invariant descriptor:*** *the discrete curvature formulation of InShaDe descriptor is by design invariant to rotations (middle row), while the derive frequency-based energy descriptors are invariant also with respect to shift (bottom row).*

We would like to remind here that, according to the Nyquist theorem, the number of contour regular samples S after the smoothing and resampling process affects the number of harmonics N necessary to reconstruct the contour curvature without adding noise

$\left(N \leq \frac{s}{2}\right)$. Finally, in order to obtain shift-invariance, we compute harmonic energies through the Euclidean norm of the harmonic coefficients [KFR03], resulting in the following Curvature Fourier Descriptor,

$$K(n) = \sqrt{a_n^2 + b_n^2}, \tag{16}$$

which provides a vector of shape features that can be used for various machine learning applications. Like the more commonly employed traditional Fourier transform, the elliptic Fourier transform results in a space-agnostic spectrum, thereby making our descriptor invariant under parameter shift (translation of the underlying domain). In this paper, we chose the elliptic Fourier transform over the traditional Fourier transform since its additional expressiveness resulted in better results. Figure 5 demonstrates both rotation- and shift-invariance.

4. Results

We have implemented our general shape descriptor method and tested it on several challenging use cases. In the following, we first provide details on our implementation (Sec. 4.1) and then provide an evaluation on general shape analysis and on the analysis of histopathological images.

4.1. Implementation notes

We implemented the geometry processing pipeline in Python, by using the following packages: G-U-Net [CTT*19] for automatic segmentation, sklearn, skimage for contour processing and dimension reduction, interactive matplotlib for visualization. For testing the pipeline, we developed simple interactive widgets in which users can compare the clustering visualization in the parameter space to the reconstructed cellular shapes in the histology images. We tested the components through Jupyter notebooks on a Razer Blade Stealth laptop equipped with an Intel Core i7-1065G7 and an NVIDIA GeForce GTX 1650 Ti and connected to an eGPU NVIDIA Titan RTX. In all results presented in this paper we used the following settings: $T = 2$ iteration steps for shape smoothing, $N = 256$ for uniform resampling over the shape contours, and $K = 64$ as number of Fourier energy coefficients for representing the shapes. Moreover, in order to amplify the signal of high frequencies, we considered a frequency equalization scheme weighting the InShaDe coefficients according to the square root of the order ($w(k) = \sqrt{k}$). Our geometry processing pipeline can be easily integrated with different dimension reduction schemes and clustering methods: in this work, as dimension reduction scheme for visualizing the descriptors, we considered the very recent Uniform Manifold Approximation and Projection (UMAP) method, based on Riemannian geometry and algebraic topology [MHM18], while for clustering we used HDBSCAN [CMS13] or k-Means [AV06] according to the cases.

4.2. Evaluation

After evaluation on the classic MPEG-7 shape collection commonly used in literature for testing shape retrieval methods, we report here preliminary results obtained with our pipeline on a number of histology samples for medical diagnostics and neuroscience

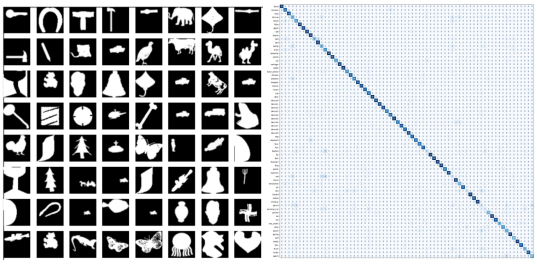

Figure 6: ***MPEG-7 experiments:*** *we test our InShaDe using the classical MPEG-7 shape collection commonly used for testing image processing algorithms (left). A simple Support Vector Machine classifier over our descriptor is able to obtain classification accuracy en-par with standard geometry-based classification methods (78% over the complete shape collection). We also show the full confusion matrix obtained on the testing data (right).*

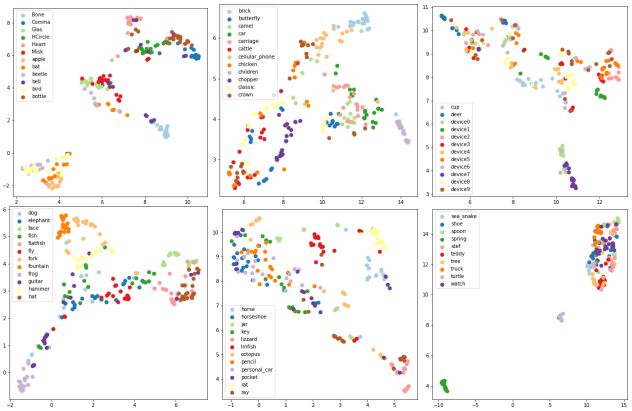

Figure 7: ***MPEG-7 UMAP clustering:*** *we test UMAP dimension reduction on the proposed invariant shape descriptor for MPEG-7 collections. In order to reduce visual cluttering, the various shapes are separated in 6 groups of maximum 12 labels.*

investigations. With respect to the latter, we involved two expert domain scientists, who also author this paper, for providing a qualitative evaluation of the method, and for getting suggestions for designing a full visual analytics framework for histology images.

Preliminary validation For obtaining a first consistency validation of the InShaDe descriptor, we used MPEG-7, which is one of the most popular datasets for evaluating and comparing the accuracy of shape retrieval methods. The MPEG-7 shape collection is composed of 1,400 binary images containing objects of 70 different classes [AFFT19] (see Fig. 6 left). Since these shape contours exhibit strong distortions, we in this case enrich our original InShaDe formulation with an additional processing step for mitigating them. To this end, we perform statistical whitening, that is, we consider Principal Component Analysis for finding a linear mapping between the shape contour and the unit circle, and we apply the inverse of the linear transform to the original shapes. In order to test the InShaDe descriptor we consider a basic Support Vector Machine scheme, trained on an augmented dataset: to this end,

from the images collection we compute randomly rotated images, numbering four times the original ones. Moreover, we use an hyperparameter optimization scheme for computing the best SVM parameters over cross-correlation accuracy, and we test the obtained model over the original collection. In Fig. 6 right, we show the confusion matrix for classification obtained through our scheme, while in Fig. 7 we show the UMAP projection of our descriptor over the various shapes (we separated in groups of 12 labels to reduce clutter). In terms of accuracy, we obtain results aligned with state of the art methods using geometric features (78% for our descriptor versus 66% for Curvature based Fourier descriptor [EgBB08], 78% for blurred shape models [EFP*09] or 78% Morphological Pattern Spectrum [SP14]). Better accuracy is obtained only with more complicated hybrid contour-based and region-based descriptors (90% for Zernicke moments with geometric features [AFFT19]). For putting these results in context, we want to remind that MPEG-7 shapes are not well suited for contour-based methods. First of all, they exhibit strong distortions that we partially mitigate by pre-processing the contours through Principal Component Analysis normalization. Secondly, and more importantly, many shapes in the collection, especially artificial objects, may contain internal features that cannot be recovered by boundary based methods. Especially artificial objects with similar contours (for example, the various classes of devices in the MPEG-7 collection) cannot be discriminated by analysing the shape contours (see Figure 7 bottom right). On the other hand, our method provides excellent accuracy for recognizing natural shapes (like animals). Given these preliminary encouraging results, showing that the proposed descriptor is consistent for classifying shapes of natural objects, we are confident that the formulation can provide an adequate support for the analysis of biomedical images.

Histopathology visual analysis For visual analysis of histopathology images, we use public domain data coming from the MoNuSeg contest [KVA*19], and the very recent PanNuke dataset [GKG*20]. The former contains 30 images from seven organs with unclassified annotations of more than 20k individual nuclei, while the latter contains more than 220K labeled nuclei from 19 different tissues and, as of writing, it represents the largest open pan-cancer histology dataset for nuclei instance segmentation and classification. Finally, we apply the pipeline to a portion of a breast sample [CHG*19] obtained from the public repository TCIA (The Cancer Imaging Archive).

Figure 8 shows some examples of images from the MoNuSeg dataset [KVA*19] labeled through our framework: specifically, we apply UMAP and k-Means for clustering all contours of the entire dataset (on top left), and represent the effects on specific images. We notice how cells with similar shape features tend to form spatial clusters, and this fact can provide additional visual information to digital pathologists for diagnosis. Further investigation is needed to understand and evaluate the clinical value, but preliminary feedback from pathologists confirmed that in various cases nuclear features and clusters can provide decisive information for recognizing specific conditions.

Figure 9 shows an illustrative example of visual analysis of breast samples from the PanNuke dataset [GKG*20]: in this case, labeling was performed partially manually and partially automatically (in red neoplastic cells, in green inflammatory cells, in orange epithelial cells). We notice how, in this case, our shape descriptor cannot adequately discriminate the various cell classes according to this taxonomy (on the left). However, the analysis of clusters or the presence of outliers in the parameter space can provide pathologists visual hints for proofreading the labeling of nuclei or evaluating the accuracy of contours (like the neoplastic nuclei on the right).

Finally we test our InShaDe descriptor on a portion of a whole slide image (WSI) composed by a 3x3 tile set of resolution 1K×1K

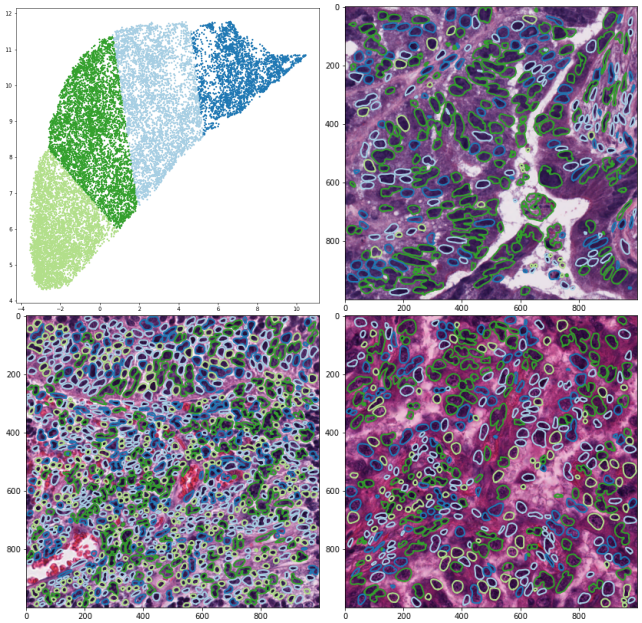

Figure 8: ***Visual clustering of histology images:*** *the InShaDe pipeline together with dimension reduction and clustering is used for visual classification. On top left, k-Means [AV06] is used to create four clusters over all nuclei segmented from the MoNuSeg dataset [KVA*19], while the other images show the effect of clustering for specific histology images. Spatial patterns created by shapes with similar features are recognizable.*

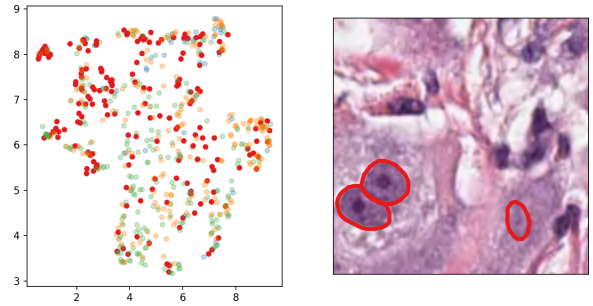

Figure 9: ***Visual analysis of PanNuke segmentation:*** *our visual analysis pipeline is used for proofreading and checking labeling of histology images. In this example, the neoplastic cell type is selected from parameter space and rendered on one of the original imagesof the PanNuke dataset [GKG*20].*

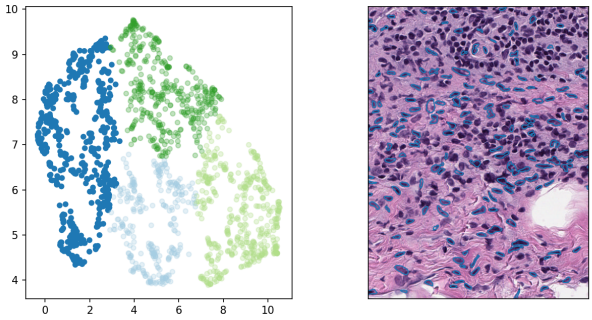

Figure 10: ***Visual analysis of WSI:*** *the InShaDe processing pipeline is applied to the analysis of Whole Slide Images (WSI). A portion of a breast sample from the dataset Breast Metastases to Axillary Lymph Nodes [CHG*19] obtained from the public repository TCIA (The Cancer Imaging Archive) is shown. Pathologists can choose a region in the parameter space (blue cluster on the left), and visualize the associated contours in the WSI (right), to check for spatial clusters or patterns.*

from a breast sample [CHG*19] obtained from the public repository TCIA (The Cancer Imaging Archive). In this case, clustering was computed through k-Means [AV06] (left), and applied to the tiles for showing eventual spatial patterns that can match with metastatic tissues. In figure 10 we show an interactive example, in which the blue cluster is selected in the parameter space (left) and the associated contours are highlighted in the histology image (right). Pathologists can select and create clusters and regions in the parameter space, and check whether nuclei with similar shape features form specific spatial clusters in the image space.

Qualitative evaluation We tested our InShaDe processing pipeline also on biologic histology images of rodent brain samples currently used for neuroscience investigations. To this end, we involved two expert neuroscientists for providing a qualitative evaluation of the framework as applied to images obtained with different staining techniques. As a general outcome, the domain scientists were particularly impressed by the segmentation quality and they were able to map specific features in the shape features space to specific patterns in the histology images.

Specifically, in figure 11 left we show the outcomes of Nissl staining of mice brain sections: clustering was obtained with k-Means [AV06]. The Nissl staining is not specific for particular cell type and is commonly used for cell counting, since it provides an excellent contrast between the cellular and extracellular space. On the other hand, it does not provide a very good contrast between the cytoplasm and the cell nucleus. In the example reported, the contrast allowed the automated algorithm to efficiently segment cell profiles, but only few nuclei were segmented (mostly in light blue). Even in this case, the usage of the parameter space for highlighting the contour shapes in the image space provides visual hints for recognizing particular features, like blurred segmentations of soma mixed with dendrites. To this end, neuroscientists consider the framework potentially useful for proofreading the quality of the staining.

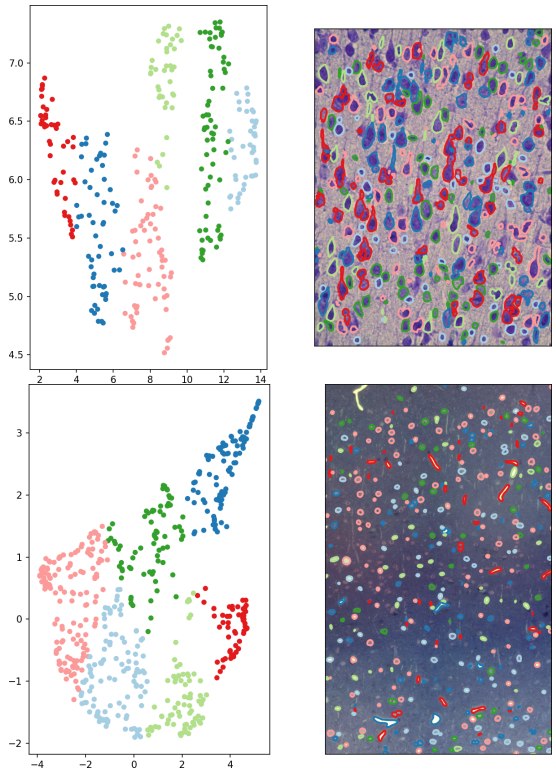

Figure 11: ***Visual analysis of mouse brain sections:*** *our visual analysis pipeline is used for a neuroscience investigation. Top: a brain section fixed with paraformaldehyde is stained with Cresyl Violet, which highlights Nissl substance in the cytoplasm of neurons. Bottom: toluidine blue is used in an attempt to discriminate nuclei from blood vessels and artifacts.*

Finally, Figure 11 right shows a portion of somatosensory cortex used on an ultrastructural work on ageing [CWB*18, ABG*18, ACAA*19]. Nuclei were stained with toluidine blue on semithin sections prepared for electron microscopy in order to count cells. The extracted contours were clustered through k-Means [AV06]. In this case, the shape feature space enabled scientists to distinguish immediately between blood vessels (in red), wrong segmentations (in blue), and nuclei from different kind of neurons (pyramidal neurons mostly in light blue and pink).

Discussion The main outcomes of our preliminary evaluation can be summarized as follows.

- **Relationships between shape parameter space and image space**: in various cases we notice that spatial clusters of cells exhibit similar shape features. Further investigation is needed to understand whether and in which cases spatial patterns or clusters in the image space correspond to patterns or clusters in the parameter space, and to associate shape clusters to specific taxonomies. In this context, we would like to remind that performing clustering on parameter space obtained after dimension reduction is still considered a complex task prone to producing unreliable results [STMT12]. Therefore, we plan to explore dif-

ferent automatic and manual dimension reduction techniques to support domain scientists during their analysis.

- **Coupling with image descriptors:** according to the analysis that we carried out on labeled data, our descriptors do not provide enough information for discriminating tumoral cells (see PanNuke dataset [GKG*20]). In order to improve classification, we plan to integrate InShaDe with sparse coding [MF13] for decomposing the inner part of nuclei as function of specific texture patterns with different physical and molecular characteristics.
- **Caveats due to staining techniques:** depending on the structure to be identified within a cell, or the type of tissue, a large plethora of immunohistochemical staining techniques are available. The proposed geometry framework can provide effective proof-reading tools for checking the quality of staining methods and semi-automatically individuating the structures of interest.
- **Taxonomy-based visual analytics system:** a real challenge in the analysis of histology images is the difficulty to individuate correct taxonomies of nuclei in order to simplify understanding and diagnosis. A visual analytics framework incorporating contour analysis, image analysis, and expert domain knowledge would help digital pathologists in labeling and proof-reading, and would provide fast ways for creating labeled data for more sophisticated artificial intelligence frameworks. To this end, our geometry processing pipeline provides encouraging results and can be easily integrated in such systems.
- **Arc-length parameterization**: While we have yet to observe our arc-length parameterization algorithm to diverge, we do not have a formal proof of convergence at the time of writing. We believe it works so well since changes in u happen very gradually and the original curve remains untouched. Each reparameterization attempt therefore slides vertices around the input curve. While formal analysis is hindered by the fact that our method is discontinuous at original vertices, we believe a full treatise to be an interesting direction for future work.

5. Conclusion

We have presented a general shape processing framework rooted in a novel differential-geometry-based descriptor of closed contours. Our descriptor provides an embedding into a fixed-dimensional feature space that can be utilized for various applications, which range from serving as input feature for deep and shallow learning techniques to supporting dimension-reduction schemes for providing a visual reference for clustering collection of shapes. While our methods are of general use, our work is motivated by the study of cellular nuclear envelopes extracted from histopathological images. In this context, we have shown the capabilities of the proposed framework for visual analysis and unsupervised classification. Our results are very encouraging, and we identify several major areas of future work in the previous section. In particular, for our specific use case, we plan to integrate our contour descriptors with texture descriptors to improve discrimination capabilities among nuclei with similar shapes but different physical and molecular characteristics. Moreover, we plan to develop, on top of our pipeline, a taxonomy-based visual analytics system to simplify study and diagnosis.

References

[ABG*18] AGUS M., BOGES D., GAGNON N., J.MAGISTRETTI P., HADWIGER M., CALÌ C.: GLAM: Glycogen-derived lactate absorption map for visual analysis of dense and sparse surface reconstructions of rodent brain structures on desktop systems and virtual environments. *Computers & Graphics 74* (August 2018), 85–98. 8

[ACAA*19] AGUS M., CALÌ C., AL-AWAMI A., GOBBETTI E., MAGISTRETTI P., HADWIGER M.: Interactive volumetric visual analysis of glycogen-derived energy absorption in nanometric brain structures. *Computer Graphics Forum 38*, 3 (2019), 427–439. 8

[AFFT19] ABBAS S., FARHAN S., FAHIEM M. A., TAUSEEF H.: Efficient shape classification using zernike moments and geometrical features on mpeg-7 dataset. *Advances in Electrical and Computer Engineering 19*, 1 (2019), 45–51. 6, 7

[AGP*20] AGUS M., GOBBETTI E., PINTORE G., CALI C., SCHNEIDER J.: Wish: Efficient 3d biological shape classification through willmore flow and spherical harmonics decomposition. In *Proceedings of the IEEE/CVF Conference on Computer Vision and Pattern Recognition Workshops* (2020), pp. 972–973. 5

[AV06] ARTHUR D., VASSILVITSKII S.: *k-means++: The advantages of careful seeding*. Tech. rep., Stanford, 2006. 6, 7, 8

[AVG*19] AGUS M., VELOZ CASTILLO M., GARNICA MOLINA J. F., GOBBETTI E., LEHVASLAIHO H., MORALES TAPIA A., MAGISTRETTI P., HADWIGER M., CALÍ C.: Shape analysis of 3d nanoscale reconstructions of brain cell nuclear envelopes by implicit and explicit parametric representations. *Computers & Graphics* (2019). 5

[BAMC20] BOGES D. J., AGUS M., MAGISTRETTI P. J., CALÌ C.: Forget about electron micrographs: A novel guide for using 3d models for quantitative analysis of dense reconstructions. In *Volume Microscopy*. Humana, New York, NY, 2020, pp. 263–304. 1

[Bob15] BOBENKO A. I.: Geometry ii: Discrete differential geometry, 2015. URL: http://page.math.tu-berlin.de/~bobenko/Lehre/Skripte/DDG_Lectures.pdf. 2, 3, 4

[BSSZ08] BOBENKO A. I., SULLIVAN J. M., SCHRÖDER P., ZIEGLER G.: *Discrete differential geometry*, vol. 38. Springer, 2008. 2

[BTU04] BLU T., THÉVENAZ P., UNSER M.: Linear interpolation revitalized. *IEEE Trans. on Image Proc. 13*, 5 (2004), 710–719. 4, 5

[CFG*15] CHANG A. X., FUNKHOUSER T., GUIBAS L., HANRAHAN P., HUANG Q., LI Z., SAVARESE S., SAVVA M., SONG S., SU H., ET AL.: Shapenet: An information-rich 3d model repository. *arXiv preprint arXiv:1512.03012* (2015). 2

[CHG*19] CAMPANELLA G., HANNA M. G., GENESLAW L., MIRAFLOR A., SILVA V. W. K., BUSAM K. J., BROGI E., REUTER V. E., KLIMSTRA D. S., FUCHS T. J.: Clinical-grade computational pathology using weakly supervised deep learning on whole slide images. *Nature medicine 25*, 8 (2019), 1301–1309. 7, 8

[CMS13] CAMPELLO R. J., MOULAVI D., SANDER J.: Density-based clustering based on hierarchical density estimates. In *Pacific-Asia conf. on knowledge discovery and data mining* (2013), pp. 160–172. 6

[CTT*19] CHIDESTER B., TON T.-V., TRAN M.-T., MA J., DO M. N.: Enhanced rotation-equivariant u-net for nuclear segmentation. In *Proceedings of the IEEE Conference on Computer Vision and Pattern Recognition Workshops* (2019), pp. 0–0. 1, 3, 6

[CW16] COHEN T., WELLING M.: Group equivariant convolutional networks. In *International conference on machine learning* (2016), pp. 2990–2999. 3

[CW17] CRANE K., WARDETZKY M.: A glimpse into discrete differential geometry. *Notices of the American Math. Soc. 64*, 10 (2017). 2

[CWB*18] CALÌ C., WAWRZYNIAK M., BECKER C., MACO B., CANTONI M., JORSTAD A., NIGRO B., GRILLO F., DE PAOLA V., FUA P., ET AL.: The effects of aging on neuropil structure in mouse somatosensory cortex—a 3d electron microscopy analysis of layer 1. *Plos One* (2018). 8

[DZPG89] DIAZ G., ZUCCARELLI A., PELLIGRA I., GHIANI A.: Elliptic fourier analysis of cell and nuclear shapes. *Computers and biomedical research 22*, 5 (1989), 405–414. 5

[EFP*09] ESCALERA S., FORNÉS A., PUJOL O., RADEVA P., SÁNCHEZ G., LLADÓS J.: Blurred shape model for binary and grey-level symbol recognition. *Pattern Recognition Letters 30*, 15 (2009), 1424–1433. 7

[EgBB08] EL-GHAZAL A., BASIR O., BELKASIM S.: A novel curvature-based shape fourier descriptor. In *2008 15th IEEE International Conf. on Image Processing* (2008), IEEE, pp. 953–956. 2, 7

[EgBB12] EL-GHAZAL A., BASIR O., BELKASIM S.: Invariant curvature-based fourier shape descriptors. *Journal of Visual Communication and Image Representation 23*, 4 (2012), 622–633. 2

[GKB*19] GAMPER J., KOOHBANANI N. A., BENET K., KHURAM A., RAJPOOT N.: Pannuke: an open pan-cancer histology dataset for nuclei instance segmentation and classification. In *European Congress on Digital Pathology* (2019), Springer, pp. 11–19. 1

[GKG*20] GAMPER J., KOOHBANANI N. A., GRAHAM S., JAHANIFAR M., KHURRAM S. A., AZAM A., HEWITT K., RAJPOOT N.: Pannuke dataset extension, insights and baselines. *arXiv preprint arXiv:2003.10778* (2020). 2, 3, 7, 9

[Got00] GOTTSCHALK S.: Collision queries using oriented bounding boxes, 2000. 3

[IVRR13] IRSHAD H., VEILLARD A., ROUX L., RACOCEANU D.: Methods for nuclei detection, segmentation, and classification in digital histopathology: a review—current status and future potential. *IEEE reviews in biomedical engineering 7* (2013), 97–114. 2

[JR17] JOTHI J. A. A., RAJAM V. M. A.: A survey on automated cancer diagnosis from histopathology images. *Artificial Intelligence Review 48*, 1 (2017), 31–81. 2

[KFR03] KAZHDAN M., FUNKHOUSER T., RUSINKIEWICZ S.: Rotation invariant spherical harmonic representation of 3D shape descriptors. In *Proc. SGP* (2003), pp. 156–164. 5, 6

[KG82] KUHL F. P., GIARDINA C. R.: Elliptic fourier features of a closed contour. *Computer graphics and image processing 18*, 3 (1982), 236–258. 5

[KH90] KHOTANZAD A., HONG Y. H.: Invariant image recognition by zernike moments. *IEEE Transactions on pattern analysis and machine intelligence 12*, 5 (1990), 489–497. 2

[KJ*18] KURNIANGGORO L., JO K.-H., ET AL.: A survey of 2d shape representation: Methods, evaluations, and future research directions. *Neurocomputing 300* (2018), 1–16. 1, 2

[KVA*19] KUMAR N., VERMA R., ANAND D., ZHOU Y., ONDER O. F., TSOUGENIS E., CHEN H., HENG P.-A., LI J., HU Z., ET AL.: A multi-organ nucleus segmentation challenge. *IEEE transactions on medical imaging 39*, 5 (2019), 1380–1391. 3, 7

[LC87] LORENSEN W. E., CLINE H. E.: Marching cubes: A high resolution 3d surface construction algorithm. *ACM siggraph computer graphics 21*, 4 (1987), 163–169. 3

[LTN06] LAGA H., TAKAHASHI H., NAKAJIMA M.: Spherical wavelet descriptors for content-based 3d model retrieval. In *IEEE International Conference on Shape Modeling and Applications 2006 (SMI'06)* (2006), IEEE, pp. 15–15. 2

[MF13] MAKHZANI A., FREY B.: K-sparse autoencoders. *arXiv preprint arXiv:1312.5663* (2013). 9

[MHM18] MCINNES L., HEALY J., MELVILLE J.: Umap: Uniform manifold approximation and projection for dimension reduction. *arXiv preprint arXiv:1802.03426* (2018). 2, 6

[MKJ08] MINGQIANG Y., KIDIYO K., JOSEPH R.: A survey of shape feature extraction techniques. *Pattern recognition 15*, 7 (2008), 43–90. 2

[ML16] MADABHUSHI A., LEE G.: Image analysis and machine learning in digital pathology: Challenges and opportunities. *Medical Image Analysis 33* (2016), 170 – 175. 1

[Mok95] MOKHTARIAN F.: Silhouette-based isolated object recognition through curvature scale space. *IEEE Transactions on Pattern Analysis and Machine Intelligence 17*, 5 (1995), 539–544. 2

[MOL01] MUKUNDAN R., ONG S., LEE P. A.: Image analysis by tchebichef moments. *IEEE Transactions on image Processing 10*, 9 (2001), 1357–1364. 2

[NFL*19] NAGPAL K., FOOTE D., LIU Y., CHEN P.-H. C., WULCZYN E., TAN F., OLSON N., SMITH J. L., MOHTASHAMIAN A., WREN J. H., ET AL.: Development and validation of a deep learning algorithm for improving gleason scoring of prostate cancer. *NPJ digital medicine 2*, 1 (2019), 1–10. 2

[RFB15] RONNEBERGER O., FISCHER P., BROX T.: U-net: Convolutional networks for biomedical image segmentation. In *International Conference on Medical image computing and computer-assisted intervention* (2015), Springer, pp. 234–241. 2, 3

[RRDM08] ROHDE G. K., RIBEIRO A. J., DAHL K. N., MURPHY R. F.: Deformation-based nuclear morphometry: Capturing nuclear shape variation in hela cells. *Cytometry Part A: The Journal of the International Society for Analytical Cytology 73*, 4 (2008), 341–350. 2

[SA20] SCHNEIDER J., AGUS M.: Reflections on the clinical acceptance of artificial intelligence. In *Multiple Perspectives on Artificial Intelligence in Healthcare: From Challenges to Opportunities*, Househ M., Kushniruk A., Borycki E., (Eds.). SpringerBriefs, 2020, p. to appear. 3

[SBR16] SINHA A., BAI J., RAMANI K.: Deep learning 3D shape surfaces using geometry images. In *Proc. ECCV* (2016), Springer, pp. 223–240. 2

[SLB*00] SHU H., LUO L., BAO X., YU W., HAN G.: An efficient method for computation of legendre moments. *Graphical Models 62*, 4 (2000), 237–262. 2

[SM06] SHEN L., MAKEDON F.: Spherical mapping for processing of 3d closed surfaces. *Image and vision comput. 24*, 7 (2006), 743–761. 5

[SP14] SHEKAR B., PILAR B.: Shape representation and classification through pattern spectrum and local binary pattern–a decision level fusion approach. In *2014 Fifth International Conference on Signal and Image Processing* (2014), IEEE, pp. 218–224. 7

[STMT12] SEDLMAIR M., TATU A., MUNZNER T., TORY M.: A taxonomy of visual cluster separation factors. In *Computer Graphics Forum* (2012), vol. 31, Wiley Online Library, pp. 1335–1344. 8

[TJL*20] TAJBAKHSH N., JEYASEELAN L., LI Q., CHIANG J. N., WU Z., DING X.: Embracing imperfect datasets: A review of deep learning solutions for medical image segmentation. *Medical Image Analysis* (2020), 101693. 2, 3

[WLG*17] WANG P.-S., LIU Y., GUO Y.-X., SUN C.-Y., TONG X.: O-cnn: Octree-based convolutional neural networks for 3d shape analysis. *ACM TOG 36*, 4 (2017), 72. 2

[WSK*15] WU Z., SONG S., KHOSLA A., YU F., ZHANG L., TANG X., XIAO J.: 3d shapenets: A deep representation for volumetric shapes. In *Proc. CVPR* (2015), pp. 1912–1920. 2

[XL08] XU D., LI H.: Geometric moment invariants. *Pattern recognition 41*, 1 (2008), 240–249. 2

[XY16] XING F., YANG L.: Robust nucleus/cell detection and segmentation in digital pathology and microscopy images: a comprehensive review. *IEEE reviews in biomedical engineering 9* (2016), 234–263. 2

[YSGG17] YI L., SU H., GUO X., GUIBAS L. J.: Syncspeccnn: Synchronized spectral cnn for 3d shape segmentation. In *Proc. CVPR* (2017), pp. 2282–2290. 2

[ZL03] ZHANG D., LU G.: A comparative study of curvature scale space and fourier descriptors for shape-based image retrieval. *Journal of Visual Communication and Image Representation 14*, 1 (2003), 39–57. 2